

Simultaneous Measurement of Ocean Winds and Waves with an Airborne Coherent Real Aperture Radar

William J. Plant
William C. Keller
Kenneth Hayes

Applied Physics Laboratory, University of Washington
Seattle, WA

July 15, 2002

Abstract

A coherent, X-band, airborne radar has been developed to measure wind speed and direction simultaneously with directional wave spectra on the ocean. The radar, called CORAR for COherent Real Aperture Radar, measures received power, mean Doppler shifts, and mean Doppler bandwidths from small resolution cells on the ocean surface and converts them into measurements of winds and waves. The system operates with two sets of antennas, one rotating and one looking to the side of the airplane. The rotating antennas yield neutral wind vectors at a height of 10 m above the ocean surface using a scatterometer model function to relate measured cross sections to wind speed and direction. The sidelooking antennas produce maps of normalized radar cross section and line-of-sight velocity from which directional ocean wave spectra may be obtained. Capabilities of CORAR for wind and wave measurement are illustrated using data taken during the Shoaling Waves EXperiment (SHOWEX) sponsored by the Office of Naval Research. Wind vectors measured by CORAR agree well with those measured by nearby buoys. Directional wave spectra obtained by CORAR illustrate that offshore winds can produce dominant waves at an angle to the wind vector that are in good agreement with the measurements. The best agreement is produced using the JONSWAP parameterizations of the development of wave height and period with fetch.

1 Introduction

An X-band airborne Coherent Real Aperture Radar, CORAR, has been developed to provide simultaneous measurements of winds and waves on the ocean surface. The system operates at moderate incidence angles where backscatter depends strongly on wind speed. It is a coherent system in which surface velocities are used to infer wave height rather than scattered power or the time of flight of a pulse to the surface as is more common [Kenny,et.al., 1979; Jackson, 1980; Hauser,et.al., 1992; Wright, et.al., 2001]. The radar was developed under funding from

the U.S. Office of Naval Research (ONR) and has been flown on a DeHavilland Twin Otter airplane during ONR's Shoaling Waves Experiment (SHOWEX).

CORAR operates in two modes, rotating and fixed, sidelooking. In both modes, cross sections, Doppler offsets, and Doppler bandwidths are collected at multiple range bins during data acquisition. In the rotating mode, the stored cross sections are subsequently averaged over small incidence and azimuth angle bins. This produces mean cross sections as a function of azimuth angle from which wind vectors at 10 meters above the ocean surface can be calculated using a scatterometer model function. In the sidelooking mode, images of both cross sections and Doppler offsets are produced from which directional spectra may be obtained. Spectra of the Doppler offset images can be directly converted to wave height variance directional spectra and their 180° ambiguities can be removed by noting changes in different flight directions. The overall result is that wind vectors and directional ocean wave spectra can be produced simultaneously.

CORAR was flown during SHOWEX from November 10, 1999 to December 5, 1999 on the UV-18A Twin Otter operated by the Center for Interdisciplinary Remotely-Piloted Aircraft Studies (CIRPAS) of Marina, CA. In addition to CORAR and the standard CIRPAS data instrumentation, the plane carried three NOAA microwave radiometers operating at 60 GHz, 37 GHz and [23 GHz, 31 GHz], the latter being one instrument. Most flights took place at 300 m altitude with a subset of flight lines being carried out at 150 m. Each day the plane also performed two circle flights at 150 m followed by a spiral from 150 m to 30 m then back up to 300 m. Table 1 lists the times and locations of data collection for the days on which CORAR collected valid data. Also shown in Table 1 are the average wind speeds and direction during the times of the flights as obtained from the nearest NDBC buoy, number 44014.

In this paper, we discuss only CORAR. In the next section, we will describe the principles of CORAR's operation. Following this, we will give examples of measured winds and waves in Section 3, comparing them with in situ measurements where possible. Much of our attention in this paper will focus on measurements from one particular day, November 16, 1999. The simultaneous wind and waves measurements of Section 3 will show that the dominant waves on this day are not in the local wind direction. In Section 4 we discuss the behavior of waves produced by winds blowing obliquely off a shoreline. In Section 5, we will show that our measured waves are, in fact, generated by wind blowing obliquely offshore north of the measurement area. In the final section, we discuss differences between our results and those of Walsh, et.al., 1989, speculate why we do not observe waves coming from Chesapeake Bay, and mention other potential capabilities of CORAR.

2 Principles of Operation

Figure 1 shows CORAR installed on the Twin Otter. The white antennas below the door on the side of the airplane are slotted waveguide antennas 120 cm long, one operating horizontally polarized and the other vertically polarized. The rotating antennas are mounted inside the gray radome under the plane. They are two slotted waveguide antennas 45 cm

Date	Time (UTC)	Location	Wind Speed (m/s)	Wind Dir (from) (degT)
11/14	18:10-21:39	Near FRF, to 75 degW	10.8	208
11/15	18:00-21:30	Near FRF, to 75 degW	10.3	307
11/16	18:02-21:49	Near FRF, to 74.9 degW	13.5	305
11/17	18:07-22:04	Near FRF, to 74.8 degW	6.6	320
11/18	16:22-20:11	Near FRF, to 74.8 degW	1.5	317
11/19	10:46-15:33	Near FRF, to 74.8 degW	2.5	265
11/20	16:59-22:36	South to Cape Hatteris, out to Gulf Stream, then Near FRF, to 74.8 degW	2.6	133
11/21	16:32-21:18	Near FRF, to 74.8 degW	4.6	73
11/23	16:17-19:04	Near FRF, to 74.6 degW	1.6	108
11/24	16:52-19:53	Near FRF, to 74.6 degW	1.7	357
11/25	20:01-22:59	Near FRF, to 74.8 degW	1.9	152
11/26	12:03-16:00	Near FRF, to 74.6 degW	6.8	161
11/28	15:57-20:33	Near FRF, to 74.6 degW	8.0	323
11/29	15:53-19:36	Near FRF, to 74.6 degW	5.0	319
11/30	15:54-20:29	Near FRF, to 74.6 degW	14.5	326
12/03	10:58-15:53	Near FRF, to 74.6 degW	6.5	235
12/04	16:00-20:01	Near FRF, to 74.6 degW	7.5	241

Table 1: Twin Otter flight information during SHOWEX in 1999 for the days on which CORAR data were collected. FRF is the Corp of Engineers Field Research Facility at Duck, NC. Times are UTC, which is local time plus five hours.

Frequency (GHz)	9.36
Peak Transmitted Power (W)	100
Pulse Repetition Frequency per Mode (kHz)	40
Vertical Beamwidths, Φ_v (deg)	25
Sidelooking Horizontal Beamwidths, Φ_h (deg)	1.8
Rotating Horizontal Beamwidths, Φ_h (deg)	5
Range Resolution, ΔR (m)	7.5
Nominal Center Incidence Angle, θ_o (deg)	60
Rotation Rate (rpm)	15
Pulses Averaged	26
Integration Time (ms)	256
Time Between Polarization Changes (ms)	370
Samples Transformed	256

Table 2: Selected CORAR Specifications

long mounted back to back on a stabilized platform inside the radome. The pulse repetition frequency (PRF) of the radar is 80 kHz but alternate pulses go to the sidelooking and rotating antennas so the effective PRF from either antenna is 40 kHz. A switch changes between the H-pol and V-pol antenna of each system after a time interval of about 1/3 second. When collecting data for directional spectral calculations from the fixed antennas, this switching does not occur so that all data are collected at a single polarization with the sidelooking system, usually V-pol.

The system only collects copolarized data, HH and VV. A pulse width of 50 nsec is obtained by switching; no pulse compression is used in the system. In order to improve signal-to-noise ratio, N pulses are coherently averaged. Therefore, over each 1/3 second interval, the system collects data from each range bin for each mode, rotating and sidelooking, at a rate of 40/N kHz, sufficiently fast that Doppler spectra can be calculated for 100 range bins. The system is designed so that signals from the rotating antenna can be frequency-shifted, allowing the spectra to remain within the system bandwidth even when a large component of plane velocity exists along the antenna look direction. First and second moments of the Doppler spectra are calculated and stored on hard disk along with the mean received power. A single complete Doppler spectrum from a chosen range bin is also stored for each mode. Each run typically consists of 1000 scans of approximately 1/3 sec each. The first 12 scans of each run are used to record a calibration signal and to determine the system noise level. Table 2 shows selected specifications of CORAR. Auxillary information on flight parameters are recorded along with the data. An attitude and heading reference system (AHRS) is used to produce records of aircraft pitch, roll, and heading while a differential global positioning system (DGPS) yields ground speed, track, latitude, and longitude. Residual tilts from the stabilized mount of the rotating antennas are also recorded.



Figure 1: The COherent Real Aperture Radar, CORAR, mounted on the CIRPAS Twin Otter aircraft. The white 120 cm slotted waveguide antennas below the door are the fixed, side-looking antennas. Two, back-to-back, 45 cm long, slotted waveguide antennas are mounted on a stabilized, rotating mount inside the gray radome beneath the fuselage, directly behind the sidelooking antennas in these pictures.

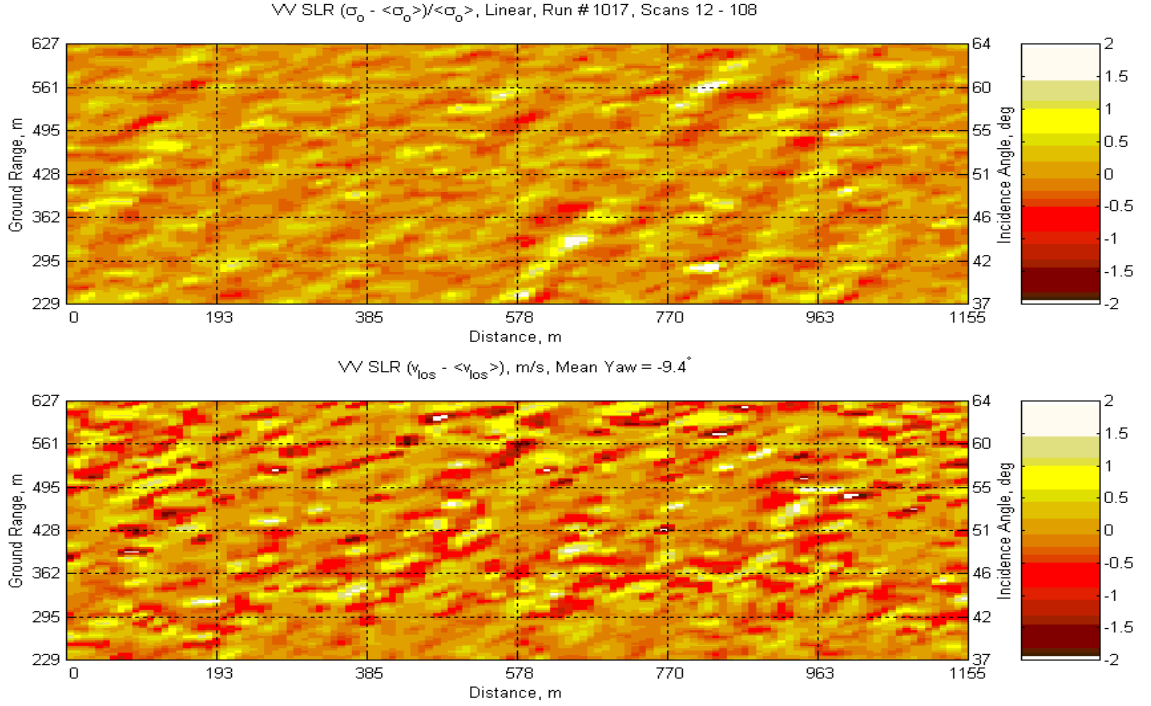


Figure 2: Images of modulated radar cross section, σ_o , and line-of-sight velocity, V_{los} obtained from CORAR's sidelooking mode.

In subsequent post-flight processing, normalized radar cross sections, σ_o , are obtained using the radar equation for each mode from the difference between the recorded mean received power and noise levels. Line-of-sight velocities are obtained from the stored first moments, f_1 , after correction for signal-to-noise ratio [Plant et.al., 1998] using the equation

$$V_{los} = \lambda f_1 / 2 \quad (1)$$

where λ is microwave length and f_1 is the first moment of the Doppler spectrum. In order to produce images having pixels in the correct positions, we needed to know the yaw of the aircraft. We found that the yaw produced by subtracting the aircraft track given by the DGPS from the heading given by the AHRS was not always accurate. Therefore, we obtained yaw from the Doppler shifts produced by our sidelooking antennas. Using the aircraft ground speed from the DGPS, we adjusted the yaw until values of f_1 calculated from ground speed, range, and yaw matched the mean value of the measured f_1 over a selected set of range bins. This yaw was then used to calculate the true surface position of each pixel and an image as a function of along and cross-track position was produced by interpolation. Figure 2 shows images of the modulated radar cross section and line-of-sight velocity modulation obtained from the sidelooking mode.

Fourier transforming the velocity modulation image and taking the magnitude squared yields the spectrum of the line-of-sight velocity as a function of encounter wavenumber,

$S_v(\vec{k}_e)$. This is a two-sided spectrum that must be corrected for the finite resolution of the system and for mapping distortion by changing the encounter wavenumber to the true wavenumber, \vec{k} . The cross-track component of these two wavenumbers is the same and the relationship of the along-track components, the x components, is given by

$$k_{xe} = k_x - \omega/V \quad (2)$$

where ω is the true wave angular frequency and V is the plane velocity. Since $\omega = \sqrt{gk \tanh kd}$ where g is gravitational acceleration and d is water depth, it is then straightforward to obtain the following equation:

$$\omega^2 = g \tanh kd \sqrt{k_e^2 + \omega^2/V^2 + 2k_{xe}\omega/V}. \quad (3)$$

This equation may be solved by letting $\vec{k} = \vec{k}_e$ in $\tanh(kd)$ and in ω on the right hand side then iteratively replacing ω on the right hand side by successive values of ω from the left hand side. Then using Eq.(2), the true relationship between \vec{k} and \vec{k}_e may be established and the true group velocity of the wave field, $c_g(\vec{k})$, can be determined. Given these, $S_v(\vec{k})$ can be computed for a wave propagating in the \vec{k} direction from

$$S_v(\vec{k}) = S_v(\vec{k}_e)/(1 - c_g \sin \phi/V) \quad (4)$$

where $\sin \phi = k_x/k$.

The spectrum of the velocity image, $S_v(\vec{k})$, was used to compute a directional wave height variance spectrum as a function of along and cross-track wavenumber, $F(\vec{k})$. The relationship is

$$F(\vec{k}) = S_v(\vec{k})/[H(\vec{k})\omega^2(\cos^2 \theta_i + \sin^2 \theta_i(k_y/k_x)^2/\tanh^2 kd)] \quad (5)$$

where H is a gain function and θ_i is the incidence angle of the image. For the range of incidence angles covered by CORAR's images, a good approximation to this equation is obtained by letting $\theta_i = 47.7^\circ$. If the illuminated areas in each range bin and the product of the plane velocity and the integration time were very small compared to surface wavelengths, then the gain function H would be one. Since neither of these conditions held, the gain function was given by

$$H(\vec{k}) = e^{-(k_x^2 \rho_a^2 + k_y^2 \rho_r^2)/2} \text{sinc}^2(k_{xe} VT/2) \quad (6)$$

where T is the integration time. Surface resolutions in the range (ρ_r) and azimuth (ρ_a) directions are given by

$$\rho_r = \frac{\Delta R}{2\sqrt{2 \ln 2} \sin \theta_i} \quad (7)$$

and

$$\rho_a = \frac{\Phi h \tan \theta_i}{2\sqrt{2 \ln 2}} \quad (8)$$

where ΔR is the range resolution, Φ is the one-way, half-power antenna horizontal beamwidth in radians, and h is the altitude. Directional slope variance spectra can now be produced by multiplying $F(\vec{k})$ by k^2 .

For surface wave lengths five times the water depth, $\tanh^2 kd \approx 0.72$. In the worst case scenario of the wave travelling in the range direction, this reduces the wave height variance spectrum by 20% over its value with $\tanh kd = 1$. Waves travelling in all other directions will be affected less than this. In consideration of this and the fact that the waves in this study were generally shorter than $5d$, we have taken $\tanh kd = 1$ in the calculations in this paper.

Removal of means from the velocity images was accomplished on a scan-by-scan basis by removing the mean of the range bins. Thus if a wave train is travelling exactly in the flight direction, it is removed from the image. This exact alignment occurs rather rarely and is obvious by a reduction in significant wave height and, perhaps, an incorrect direction for the wave train. This situation is easily detected from flights in other directions.

Cross sections from the rotating mode averaged over a small range of incidence and azimuth angles yield wind speed and direction via the standard methods of scatterometry. The averaged cross sections in the upwind direction are converted to wind speed using the model function shown in Figure 3. This model function was obtained by combining the NSCAT2 model function at wind speeds above 5 m/s with cross sections measured from an airship at low wind speeds (Plant et.al.,1998). Unlike model functions used in satellite scatterometry (Schroeder, et.al., 1982), the model function used with CORAR relates wind speed to the normalized radar cross section of the sea only for antenna directions looking into the wind. Since the antenna rotates 360° in four seconds, the aircraft moves only a very short distance (approximately 200 m) during one rotation. Thus measurement of the normalized radar cross section is made in all directions for very nearly the same wind conditions, and the upwind wind direction is determined from the direction of maximum return signal. Wind speed is then determined from the level of the radar cross section in this direction alone.

3 Measured Winds and Waves

Figure 4 compares wind speeds and directions measured by CORAR with those obtained during the same period by anemometers on NDBC buoy 44014 and the University of Miami's Romeo buoy. Locations of these buoys and a typical flight pattern for the Twin Otter are shown in Figure 5. Winds measured by CORAR at distances offshore greater than 30 km have been averaged together in Figure 4 on each day; the buoy winds are the means of those obtained during the flight times of Twin Otter on each day. Wind directions from all instruments are in very good agreement on all days on which CORAR was flown except, perhaps, for the disagreement between the NDBC and Miami buoys on November 19 and that between the Miami buoy and the other two measurements on November 25. In all cases wind directions from CORAR agreed well with those from the NDBC buoy. Wind speeds from CORAR appear to be somewhat lower than the buoy wind speeds near the first of the period. Below we will show that winds to the south of the measurement area were lower

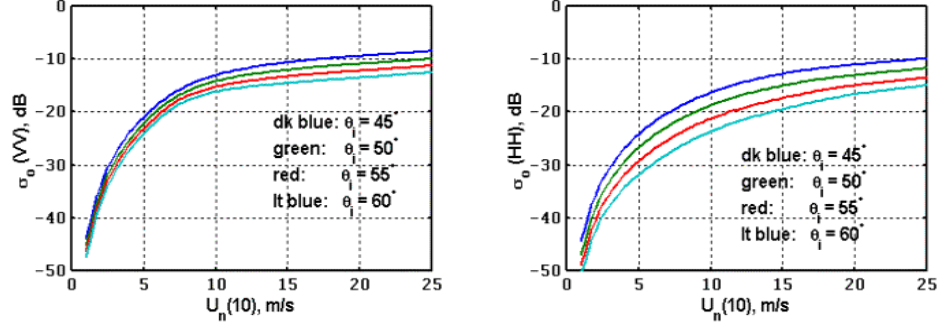


Figure 3: The model function developed for use with CORAR to convert normalized radar cross sections in the upwind direction to wind speed.

than those to the north. It is possible that the CORAR measurements were between these two wind regimes. In the center part of the period winds dropped very low and many times CORAR was unable to measure them. This is not a failing of CORAR but due to the fact that the short waves that scatter microwaves are not produced at such low wind speeds (Donelan and Pierson, 1987; Donelan and Plant, 2002). When the buoy wind speed is below about 3 m/s, very few if any data points were available from CORAR to average. Near the end of the measurement period, a time of near neutral atmospheric stability, CORAR wind speeds agree very well with those from the buoys.

Two sets of wave height and slope variance directional spectra obtained from velocity measurements using CORAR's sidelooking mode are shown in Figure 6. The two sets of measurements were made very near the point labeled 13:21 in Figure 5b but were made with the airplane flying in two different directions. The plots are oriented so that up is north and the flight direction is indicated by an arrowhead on the axis. The wavetrain apparently propagating to the north, the upper peak in all spectra, noticeably shifts in both wavelength and direction when the flight direction is changed 90°. This indicates that this wavetrain is an artifact of the fact that spectra of CORAR images are two-sided and the peak apparently propagating in the wrong direction is incorrectly shifted by the corrections for mapping distortion. This behavior allows the identification of the proper direction of wave travel in a series of wave spectra taken with different flight directions.

Figure 7 shows one of the wave height and slope variance spectra of Figure 6 with the incorrect wavetrain removed. These spectra were obtained by CORAR at 14:32 UTC on November 16, 1999. The upper plots are directional spectra while the lower plots are omnidi-

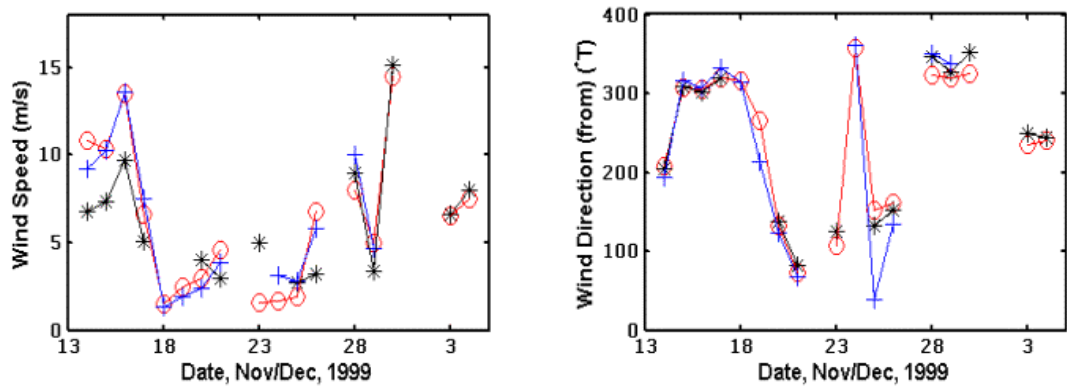


Figure 4: Wind speeds and directions measured by CORAR (asterisks) compared with those measured by NDBC buoy 44014 (circles) and the University of Miami's Romeo buoy (pluses).

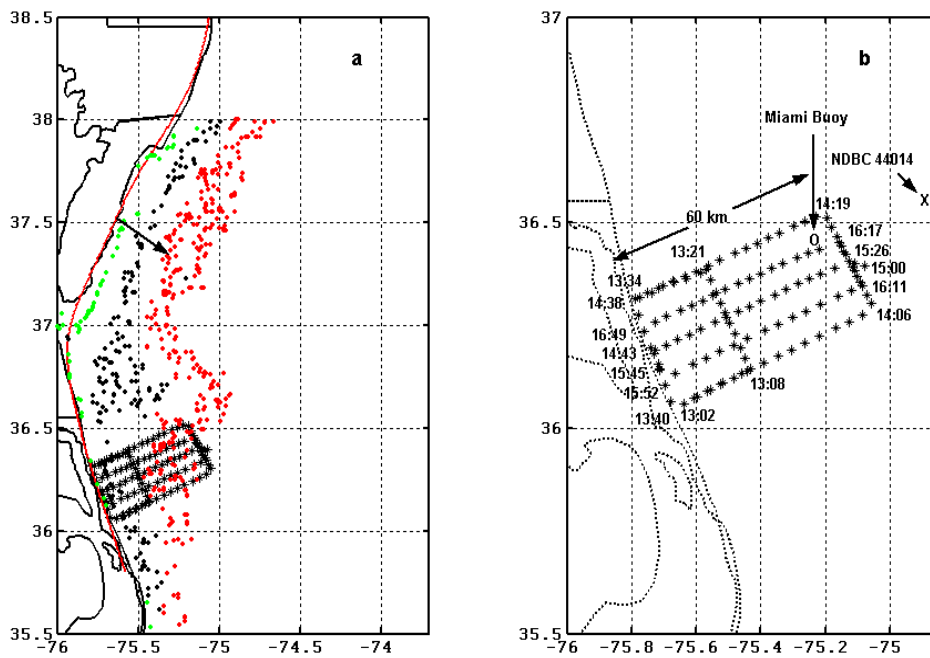


Figure 5: a) Locations of flights on November 16, 1999. Three water depths are indicated: 10 ± 0.1 m (green dots), 20 ± 0.1 m (black dots), 30 ± 0.1 m (red dots). The red curve is the smoothed coastline used for wave propagation calculations while the arrow indicates the wind direction used in those calculations. b) Locations and local times of the flights on November 16, 1999. A distance scale is shown along with the location of the University of Miami's Romeo buoy and NDBC buoy 44014.

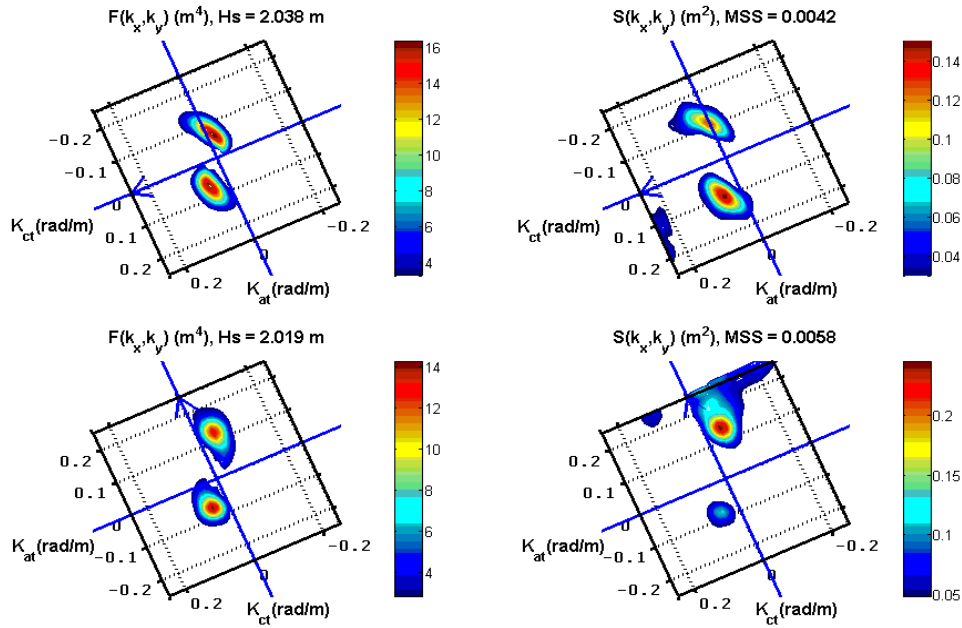


Figure 6: Comparison of wave height and slope variance directional spectra from nearby locations but different flight directions. Both locations are near 13:21 in Figure 5b and all spectra are oriented so that north is up. The plots indicate the direction toward which the waves travel; the arrowheads on the axes are in the direction of plane flight. H_s is significant wave height, MSS is the mean square slope, K_{ct} is the cross-track wavenumber, and K_{at} is the along-track wavenumber. Note that the wavenumber of the wave train traveling to the north changes in both both magnitude and direction in the different flight directions. This shows that it is the incorrect one.

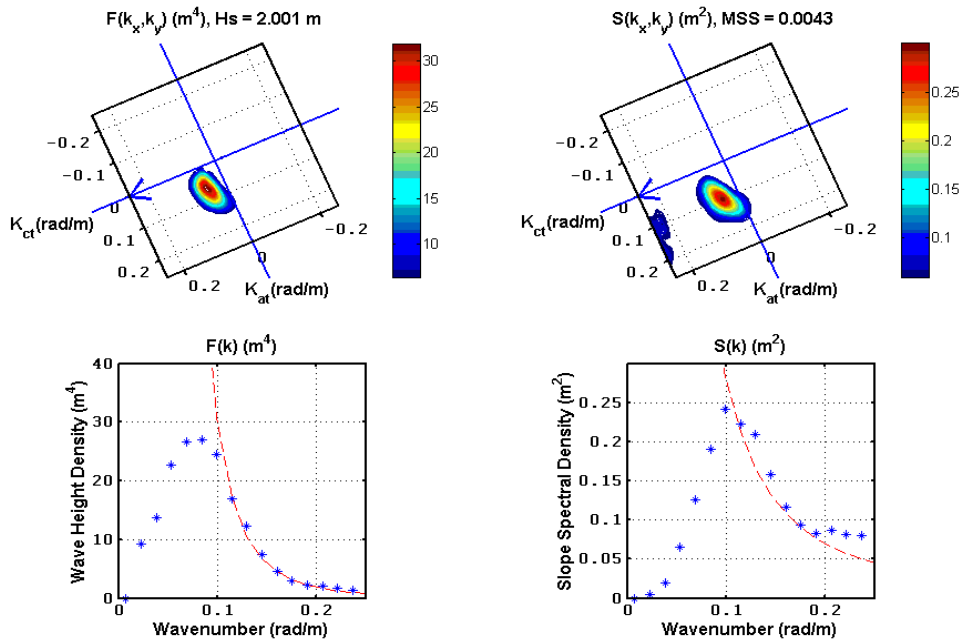


Figure 7: Wave height and slope spectra with the incorrect peak removed. Upper plots are directional spectra while the lower are the azimuthal integral of the upper ones. The dashed red lines in the lower plots are k^{-4} for the height spectra and k^{-2} for the slope spectra.

rectional spectra obtained by integrating the upper plots over all azimuth angles. Significant wave heights and mean square slopes shown in this figure should be more accurate than those in Figure 6, although the differences are not large.

We may conveniently summarize the simultaneous measurements from CORAR by plotting wind vectors and dominant wavenumber vectors. Such plots are shown in Figure 8 for the measurements made on November 16, 1999. The figure shows that winds on this day were from the northwest while the dominant waves came nearly from the north. These waves do not appear to be generated by the local wind. In the next section, we consider the possible origin of the waves.

4 Waves Produced by Oblique Offshore Winds

In their studies on Lake Ontario, Donelan et.al. (1985) (hereafter DHH) showed that winds blowing obliquely offshore at an angle to the perpendicular to the shoreline produce dominant waves that do not travel in the wind direction. DHH pointed out that the characteristics of waves in a given area depend on their development over the entire upwind fetch. Under steady state conditions, relationships have been obtained by several investigators relating the development of the dominant wave period, T_p , and the significant wave height, H_s , to

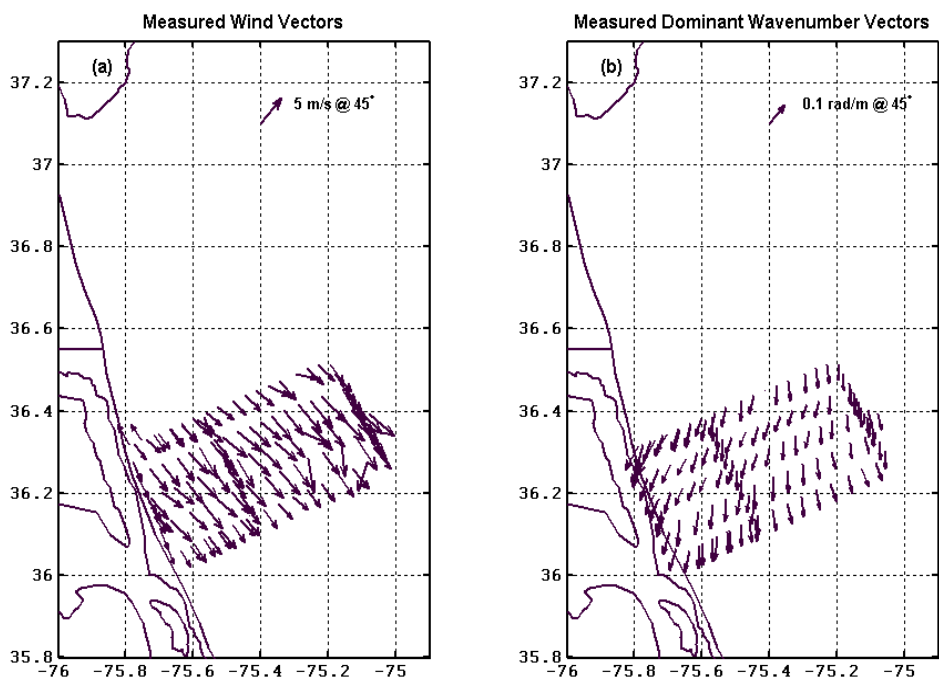


Figure 8: Wind vectors and dominant wavenumber vectors obtained by CORAR on November 16, 1999.

Reference	A	B	C X 10 ⁷	D	ρ
Hasselmann et.al. (1973)(JONSAP)	3.5	0.33	1.60	1.00	1
Donelan et.al. (1985) (DHH)	1.85	0.23	8.39	0.76	1
Walsh et.al. (1989) (WHHSS)	2.3	0.29	1.86	1.00	$(\cos \theta)^{0.63}$

Table 3: Values of parameters found by different investigators for the fetch-limited growth relations given in the text.

the wind speed and fetch. These relationships may be summarized as follows:

$$T_p = A^{-1} g^{(B-1)} X_\theta^B (U \rho \cos \theta)^{(1-2B)} \quad (9)$$

$$H_s = 4C^{1/2} X_\theta^{D/2} g^{(D-2)/2} (U \rho \cos \theta)^{(2-D)} \quad (10)$$

where U is wind speed in m/s, X_θ is the fetch in meters at an angle θ to the wind, ρ is a parameter that is one for $\theta = 0$, and A , B , C , and D are constants. While the same forms of the equations have been used by many investigators, the values of the parameters A , B , C , D , and ρ have varied for different investigations. Their values determined in several studies are given in Table 3. (We do not include values determined by Phillips (1977) and Liu and Ross (1980) since they yield incorrect behavior for the wave steepness.) In fact, these relationships were first developed for dominant waves traveling in the wind direction, that is, with $\theta = 0$ and $\rho = 1$ (Hasselmann, et.al. 1973, hereafter JONSWAP). DHH assumed that the development of waves at an angle to the wind would follow the same relationships but with the component of wind velocity in a given direction substituted for the wind speed, that is, they extended the relationships to $\theta \neq 0$ (with $\rho = 1$). The idea of DHH was that if the fetch increased sufficiently rapidly with θ to one side of the wind direction, it could cause the dominant wave period to increase, counteracting the decreasing influence of the wind, and causing the dominant wave to propagate at an angle to the wind direction. Their measurements agreed well with this idea using their values of the parameters A , B , C , and D . Walsh et.al. (1989) (hereafter WHHSS) pointed out that nonlinear interactions could also influence waves propagating at an angle to the wind and added the parameter ρ to the above equations to account for this possibility. They determined ρ by forcing their growth relationships to maximize in the same direction as those of DHH.

Although the constants in Table 3 do not appear to differ from each other by large amounts, the differences are crucial for this study. The smaller values of B and D obtained by DHH cause the dominant wave to grow more slowly with fetch than the other two formulations. Thus using the DHH formulation, waves approach full development at much longer fetches than found experimentally by WHHSS. This is important because WHHSS showed that for a straight shoreline and various angles ϕ of the wind off the perpendicular to the shoreline, the growth relations with the JONSWAP parameters yield no maximum dominant wave period for any value of θ and those of DHH yield maxima only for $\theta < 26^\circ$.

But WHHSS showed that at a sufficiently long fetch the waves approach full development where dominant wave properties no longer depend on fetch. Thus the growth relation for T_p , Eq.(9), must always reach a peak at some value of θ where the fetch is sufficiently long that T_p depends only on the decreasing component of wind velocity in the direction θ . Using the criterion of WHHSS that full development is reached when the dimensionless peak frequency ($U \rho \cos \theta / (g T_p)$) equals 0.133, we find the following dependence of T_p and H_s on $U \rho \cos \theta$ at full development:

$$T_p = U \rho \cos \theta / (0.133g) \quad (11)$$

and

$$H_s = 4C^{1/2}(A/0.133)^{D/(2B)}g^{-1}(U \rho \cos \theta)^2 \quad (12)$$

Note that DHH give the relation determining full development to be $(U \cos \theta) / c_p = 0.83$ while the above equations yield $(U \rho \cos \theta) / c_p = 0.836$ where $c_p = g T_p / (2\pi)$ is the phase speed of the dominant wave. The fetch at which full development occurs is

$$X_\theta = (A/0.133)^{1/B}g^{-1}(U \rho \cos \theta)^2. \quad (13)$$

To compare these ideas with CORAR's measurements, we needed to know the time duration, d_e , during which the wind had acted on the waves as a function of θ since the fetch from the measurement location to the shoreline depended on θ . This duration is given by

$$d_e = \int_0^{X_\theta} dX / c_g = (4\pi/g) \int_0^{X_\theta} dX / T_p \quad (14)$$

where c_g is the group speed of the dominant wave. Only if the wind is constant over this time period can the above relations be expected to hold.

5 Oblique Winds and CORAR Data

To determine the winds over the development fetch of the observed waves, we used winds measured by NDBC buoys at various locations along the coast. Locations of the buoys considered are shown in Figure 9 while wind speeds and directions from the anemometers on these buoys are shown in Figure 10 for three different days during SHOWEX on which the winds came from the northwest. The winds are plotted against the number of hours before the last flight of the day. The vertical dashed line in the plots for November 16 is the maximum duration necessary to obtain full development at the location of the last flight. Also shown in Figure 10 are the winds measured by CORAR in the SHOWEX flight area indicated in Figure 5. On November 16, winds from the buoys to the north and east of the flight area were high and rather constant in both magnitude and direction over time periods of the order of 15 hours prior to the end of flights. This period exceeded d_e for all fetches up to the full-development fetch so this day offers an excellent test of oblique-wind ideas. Winds

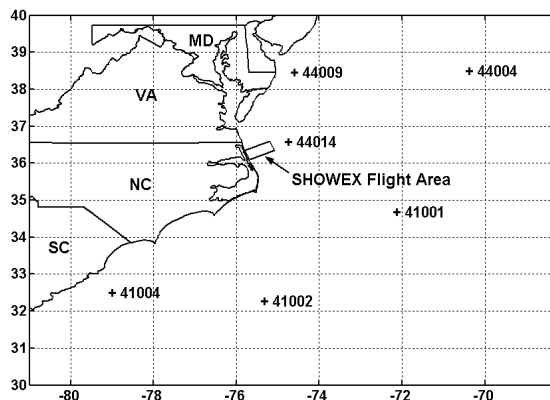


Figure 9: Location of NDBC bouys and the SHOWEX flight area.

to the south and east of the flight area on this day were lower and more variable than those to the north and east; their magnitudes also agreed better with CORAR's measurements. On November 17, winds at all buoys were decreasing over time periods relevant to the CORAR measurements. Again wind speeds at the buoys to the south and east agreed well with CORAR's measurements and were somewhat lower than those from the other buoys. Their directions were from more northerly directions than either those of CORAR or those of the north and east buoys. Because of the decreasing wind speeds, this day does not offer a good test of the wave development equations. On November 28, wind speeds from the north and east buoys, except 44009, were fairly constant for the 20 hours prior to the end of flights but wind directions at all of the near-shore buoys showed large changes in the 5 to 12 hours prior to the end of flights. Because of these direction changes, this day is also not optimum to investigate oblique-wind effects.

The considerations of the last paragraph led us to concentrate on a comparison between CORAR's wave measurements and the predicted properties of waves produced by winds blowing off the Maryland and Virginia coasts on November 16. Wind speeds and directions were taken to be those given by the horizontal dashed lines in Figure 10. The wind direction is indicated in Figure 5a. Using the smoothed version of the coastline indicated by the red curve in Figure 5a, we calculated the distance to the coastline in different directions from each location at which spectra had been obtained by CORAR. Maxima of T_p versus θ were then determined for each location. The value of θ where T_p maximized was taken to be the predicted direction of wave propagation and the value of H_s was computed from either Eq.(10) or Eq.(12). The maximum value of T_p was used to compute the peak wavenumber k_p . This calculation is not as straightforward as has previously been supposed since the same wave is not the peak of both frequency and wavenumber spectra so the relationship is not given by

$$k_p = (2\pi/T_p)^2/g. \quad (15)$$

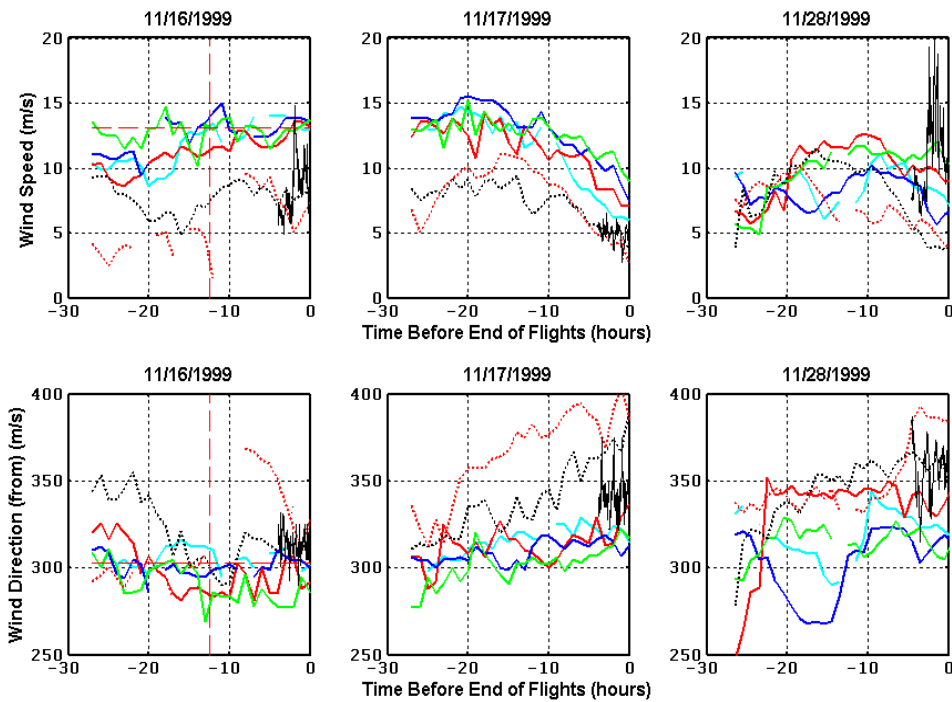


Figure 10: Wind speed and direction prior to the November 16, 1999 CORAR flights. Data sources for the various curves are as follows: solid cyan = NDBC buoy 44014, solid red = NDBC buoy 41001, solid blue = NDBC buoy 44009, solid green = NDBC buoy 44004, dotted black = NDBC buoy 41002, dotted red = NDBC buoy 41004, solid black = CORAR. Vertical dashed lines indicate the maximum time necessary for the waves to achieve full development at the wind speed indicated by the horizontal dashed line. The two horizontal dashed lines show the wind speed and direction used in the calculations of oblique-wind effects in the text.

Rather the relationship between k_p and T_p depends on the shape of the spectrum because frequency and wavenumber spectra are related by

$$F(k, \theta) = F(\omega, \theta)c_g/k \quad (16)$$

where k is wavenumber and ω is angular frequency. Therefore, k_p will be lower than that given by Eq.(15) by a non-negligible amount that depends on spectral width.

Figure 11 compares wave properties calculated by the above procedures using the JONSWAP parameters (circles) with those measured by CORAR (asterisks). The top row of plots show dominant wavenumber, dominant wave direction, and significant wave height versus distance from the nearest point of land. The lower row shows the same quantities plotted against time; locations for the values may be determined from Figure 5b. Wave directions in this figure are those toward which the waves are propagating and indicate that the largest waves in the SHOWEX area on November 16, 1999 originated just south of the southern tip of Assateague Island, which runs along the Maryland/Virginia coast. Dominant wave numbers measured by CORAR agree almost perfectly with the predicted ones in both their dependence on offshore distance and on time. Wave directions and significant wave heights agree well at the most distant locations from the shoreline but disagree closer to the coast. Two refraction effects may be responsible for the differences near shore. First, close to the North Carolina shoreline, the water depth is below 20 meters for offshore distances less than about 20 km. Since the predicted dominant waves are about 80 m long, the waves will be refracted toward the shore normal as they propagate toward the coast. This is consistent with the observed directional differences and also with the lower observed significant wave heights near shore. Second, as Figure 5a shows, waves propagating from their source to these near-shore measurement locations pass over an area where the bottom is about 20 m deep. Again this is shallow enough that the growing waves may be refracted and lose some energy.

We also compared our directional wave measurements with predictions using the parameters of DHH and WHHSS. The results are shown in Figure 12. Both sets of parameters predict dominant waves shorter than those measured. Propagation directions for the dominant waves are also farther from those measured than was the case for the JONSWAP parameters. Only significant wave heights for the DHH parameters are perhaps a better fit to the data than those produced by the JONSWAP parameters.

6 Discussion and Conclusion

The predicted dominant wave directions for the DHH and WHHSS parameters are identical in Figure 12. This is not an accident. WHHSS set their value of ρ by forcing their parameterization to yield the same dominant wave directions as DHH. They also adjusted ρ for the JONSWAP parameters to force this parameterization to yield DHH's dominant wave directions. When we compare our results with these adjusted JONSWAP parameters we find that the comparison is very similar to that with the WHHSS parameters and not as good as those obtained using the original JONSWAP parameters.

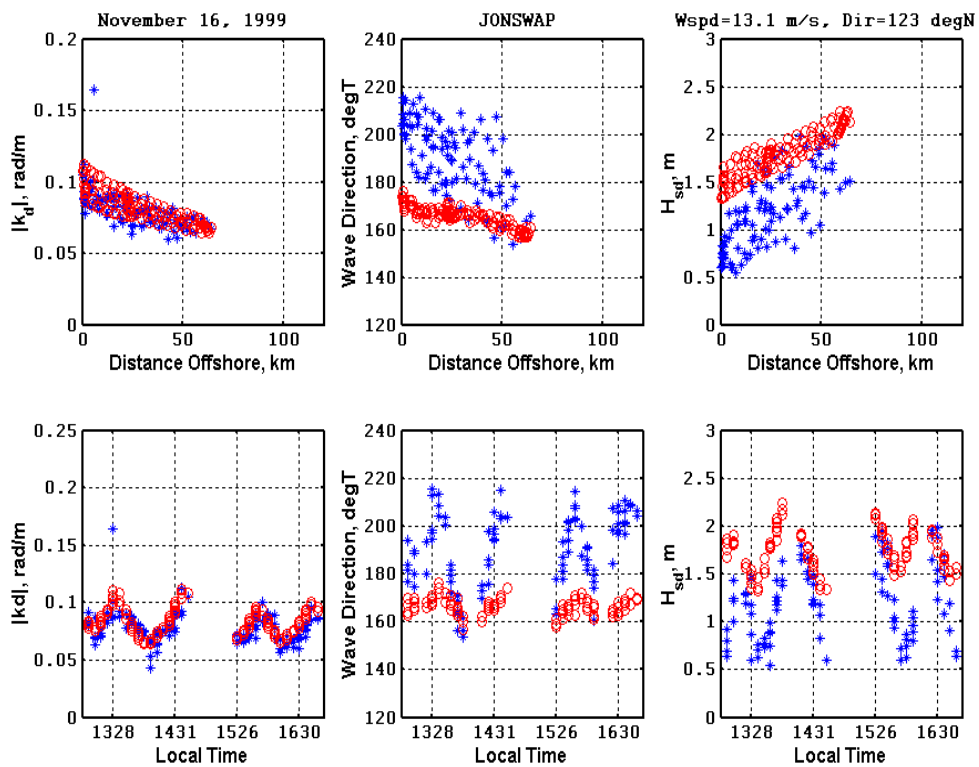


Figure 11: Comparison of wave measurements on November 16, 1999 (red circles) with those expected to be produced by winds blowing obliquely off the Maryland/Virginia coast using the JONSWAP growth parameters (blue asterisks).

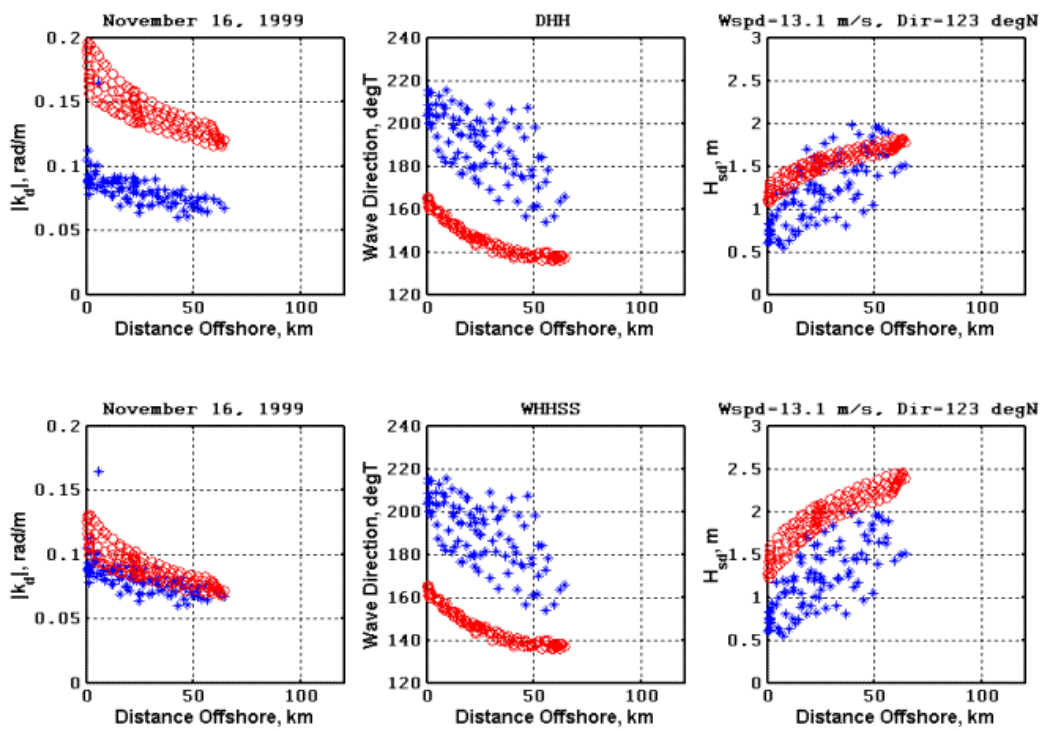


Figure 12: Comparison of wave measurements on November 16, 1999 with those expected to be produced by winds blowing obliquely off the Maryland/Virginia coast using DHH (top row) and WHHSS (bottom row) growth parameters. Red circles are predictions and blue asterisks are measurements.

The results presented here are different from those of WHHSS in some respects but agree with them in other respects. WHHSS found that JONSWAP parameters yielded a much better fit to the development of their significant wave heights and dominant wavenumbers than DHH parameters did. This agrees with our findings. On the other hand, WHHSS found that Donelan's parameters fit their wave directions better for the oblique wind conditions of their experiment, which disagrees with our result.

The apparent absence in our data set of waves coming from the mouth of Chesapeake Bay is at first glance surprising. However, if dominant waves in the bay also propagate at angles to the wind, they would not propagate out the mouth of the bay but would be incident on the beach to the west of the mouth. This may be the reason that waves from the bay are not apparent in our data.

The measurements presented here show that CORAR can simultaneously measure wind vectors and directional wave spectra with good accuracy. To date, we have obtained wave spectra only from images of surface velocity produced by the system in the sidelooking mode. In principle it should also be possible to obtain directional spectra also from the cross section measurements in the sidelooking mode as well as from both the cross section and velocity measurements in the rotating mode. Due to instrument problems during the flights, we have not been able to attempt to extract wave spectra from the rotating mode velocity measurements. We have attempted to extract wave height and slope spectra from the modulations of cross section in both modes but have not been able to obtain consistent results. It may be that waves are not the only modulating influences on the measured cross sections. We intend to pursue the determination of directional wave spectra from these alternate methods in the future.

7 Acknowledgments

The authors would like to thank Len Fedor and Brad Fisk for arranging the construction of the radome for the rotating antennas. We also want to thank CIRPAS personnel for their competence and cooperation throughout the project. This work was supported by ONR Grant # N00014-97-1-0478.

8 References

Donelan, M.A., J. Hamilton, and W.H. Hui, 1985. Directional spectra of wind-generated waves. *Phil. Trans. R. Soc. Lond.*, **315**, pp. 509-562.

Donelan, M.A. and W.J. Pierson, Radar scattering and equilibrium ranges in wind-generated waves with application to scatterometry, *J. Geophys. Res.*, 93(C5), 4871-5029, 1987.

Donelan, M.A., and W.J. Plant, Threshold and hysteresis effects in wind wave growth and decay. Part 1: gravity-capillary waves, submitted to *J. Phys. Ocean.*, 2002.

Hauser, D., G. Caudal, G.J. Rijckenberg, D. Vidal-Madjar, G. Laurent, and P. Lancelin, RESSAC: A new airborne FM/CW radar ocean wave spectrometer, *IEEE Trans. Geosci. Remote Sensing*, 30(5), 981-995, 1992.

Hasselmann, K., T.P. Barnett, E. Bouws, H. Carlson, D.E. Cartwright, K. Enke, J.A. Ewing, H. Gienapp, D.E. Hasselmann, P. Kruseman, A. Meerburg, P. Müller, D. J. Olbers, K. Richter, W. Sell, H. Walden, Measurements of wind-wave growth and swell decay during the joint North Sea wave project. (JONSWAP), *Ergänzungsheft zur Deutschen Hydrograph. Zeitschrift, Reihe A* (8⁰)(12), 95 p, 1973.

Jackson, F.C., An analysis of short pulse and dual frequency radar techniques for measuring ocean wave spectra from satellites, *Radio Sci.*, 16(6), 1385-1400, 1980.

Kenny, J. E., E.A. Uliana, and E.J. Walsh, The surface contour radar, a unique radar remote sensing instrument. *IEEE Trans., Microwave Theory and Tech.*, MTT-27(12), 1080-1092, 1979.

Liu, P.C., and D.B. Ross, Airborne measurements of wave growth for stable and unstable atmospheres in Lake Michigan, *J. Phys. Ocean.*, 11, 1842-1853, 1980.

Phillips, O.M., *The Dynamics of the Upper Ocean*, 2nd ed., Cambridge University Press, 336 pp, 1977.

Plant, W.J., W.C. Keller, V. Hesany, and K. Hayes, Measurements of the marine boundary layer from an airship, *J. Atmos. Ocean. Tech.*, 15, 1433-1458, 1998.

Schroeder, L.C., D.H. Boggs, G. Dome, I.M. Halberstam, W.L. Jones, W.J. Pierson, and F.J. Wentz, The relationship between wind vector and normalized radar cross section used to derive SEASAT-A satellite scatterometer winds, *J. Geophys. Res.*, 87(C5), 3318-3336, 1982.

Walsh, E.J., D.W. Hancock III, D.E. Hines, R.N. Swift, and J.F. Scott, An observation of the directional wave spectrum evolution from shoreline to fully developed, *J. Phys. Oceanogr.*, 19, 670-690, 1989.

Wright C.W., E.J. Walsh, D. Vandemark , W.B. Krabill, A.W. Garcia, S.H. Houston, M.D. Powell, P.G. Black, F.D. Marks, Hurricane directional wave spectrum spatial variation in the open ocean. *J Phys. Ocean.*, 31(8), 2472-2488, 2001.